Chemical Science

ROYAL SOCIETY OF CHEMISTRY

EDGE ARTICLE

View Article Online
View Journal | View Issue

Cite this: *Chem. Sci.*, 2023, **14**, 1787

All publication charges for this article have been paid for by the Royal Society of Chemistry

From amorphous to crystalline: a universal strategy for structure regulation of high-entropy transition metal oxides†

Dawei Lai,‡[a] Li Ling,‡[a] Mengfei Su,[b] Qiaoling Kang,[bc] Feng Gao *[a] and Qingyi Lu *[b]

High-entropy materials (HEMs) exhibit extensive application potential owing to their unique structural characteristics. Structure regulation is an effective strategy for enhancing material performance. However, the fabrication of HEMs by integrating five metal elements into a single crystalline phase remains a grand challenge, not to mention their structure regulation. Herein, an amorphous-to-crystalline transformation route is proposed to simultaneously achieve the synthesis and structure regulation of high-entropy metal oxides (HEMOs). Through a facile hydrothermal technique, five metal sources are uniformly integrated into amorphous carbon spheres, which are transformed to crystalline HEMOs after calcination. Importantly, by controlling ion diffusion and oxidation rates, HEMOs with different structures can be controllably achieved. As an example, HEMO of the five first-row transition metals CrMnFeCoNiO is synthesized through the amorphous-to-crystalline transformation route, and structure regulation from solid spheres to core–shell spheres, and then to hollow spheres, is successfully realized. Among the structures, the core–shell CrMnFeCoNiO exhibits enhanced lithium storage performance due to the component and structural advantages. Our work expands the synthesis methods for HEMs and provides a rational route for structure regulation, which brings them great potential as high-performance materials in energy storage and conversion.

Received 2nd September 2022
Accepted 11th January 2023

DOI: 10.1039/d2sc04900g

rsc.li/chemical-science

Introduction

Lithium-ion batteries (LIBs) have been widely used in the fields of new-energy electric vehicles, portable electronic devices, and short to mid-term stationary energy storage, occupying a great share in the highly competitive battery market.[1–4] A conventional lithium-ion battery typically consists of a modified carbon-based anode and a lithium transition metal oxide-based cathode.[5–7] In the face of rapid developments in science and technology, these traditional LIB electrode materials are increasingly unable to meet the demanding requirements for capacity, energy density, safety, size and cost.[8–10] Therefore, the exploration of new LIB electrode materials and the realization of their structure and composition design are highly desirable for developing high-performance LIBs.[11–14]

High-entropy materials represent a new kind of material consisting of at least five metal elements in a near-equimolar proportion, deliberately incorporated into a single crystalline phase.[15–17] They include high-entropy alloys (HEAs) and high-entropy compounds and have attracted increasing interest in recent years because the unconventional compositions and crystalline structures hold promise for achieving unprecedented performance.[18–20] In energy storage and conversion fields, high-entropy material electrodes exhibit superior cell activity with excellent stability.[21,22] In comparison to the significant attention and research on HEAs, few reports on high-entropy compounds have been documented, because it is more difficult to form high-entropy compounds with a single phase than high-entropy alloys, due to the incompatibility among different metals and nonmetals.[20–23] Additionally, the current synthesis strategies for high-entropy compounds are complicated, cumbersome, and costly.[23,24]

In 2015, Rost *et al.* first explored and created an entropy-stable oxide (ESO) that is thermodynamically similar to HEAs but represents a new material, called high-entropy metal oxide (HEMO).[25] Different from HEAs formed by metal bond connection, HEMOs contain covalent and ionic bonds. Though

[a]*Department of Materials Science and Engineering, Jiangsu Key Laboratory of Artificial Functional Materials, Collaborative Innovation Center of Advanced Microstructures, College of Engineering and Applied Sciences, Nanjing University, Nanjing 210023, P. R. China. E-mail: fgao@nju.edu.cn*

[b]*State Key Laboratory of Coordination Chemistry, Coordination Chemistry Institute, Collaborative Innovation Center of Advanced Microstructures, School of Chemistry and Chemical Engineering, Nanjing University, Nanjing 210023, P. R. China. E-mail: qylu@nju.edu.cn*

[c]*College of Materials and Chemistry, China Jiliang University, Hangzhou 310018, P. R. China*

† Electronic supplementary information (ESI) available. See DOI: https://doi.org/10.1039/d2sc04900g

‡ These authors contributed equally to the work.

the crystal structure stability of HEMOs is lower than that of HEAs, the addition of anionic sublattice makes the crystal structure wider and results in greater functional diversity. As high-entropy compounds, HEMOs exhibit the properties of both oxides and high entropy, features and characteristics that perfectly meet the requirements for the structure and composition design of electrode materials for transition metal oxide LIBs.[26] Thus, researchers are increasingly active in the research of high-entropy oxides for energy storage and conversion. To date, many research groups have synthesized high-entropy oxides as electrode materials for LIBs that show good performance and great cycling stability, but the rigorous synthesis conditions, high cost, and cumbersome process greatly hinder their development and applications.[27–29]

Moreover, it is known that material properties have a strong structural dependence. Structure regulation is one of the most effective means to construct more active sites to improve properties and thus enhance performance. At present, it is still a great challenge to realize the facile synthesis of high-entropy compounds, not to mention structure regulation. So far, most of the synthesized high-entropy compounds including HEMOs are nanoparticles, which always suffer from disorderly aggregations. Achieving structure regulation of high-entropy compounds will further improve their performance and expand their applications. Herein, an amorphous-to-crystalline transformation strategy is proposed for the simultaneous achievement of the synthesis of high-entropy transition metal oxides and regulation of their structure. In this strategy, two facile synthesis methods, hydrothermal technique and calcined oxidation process, are combined. Through the former, amorphous carbon spheres incorporated with five metal species are acquired, which are oxidized and transformed to crystalline HEMOs by the latter. Importantly, during the oxidation process, the structure evolution of HEMOs from solid spheres (s-HEMO) to core–shell spheres (c-HEMO), and then to hollow spheres (h-HEMO) can be controllably achieved by adjusting the calcination temperature to vary the ion diffusion and oxidation rates. This amorphous-to-crystalline transformation route is universal for HEMOs, and CrMnFeCoNiO materials with the five first-row transition metals are discussed in detail as an example. When used as LIB anode, the core–shell high-entropy CrMnFeCoNiO (c-CrMnFeCoNiO) exhibits the best lithium storage performance, with a high specific capacity of 968.5 mA h g^{-1} and outstanding cycling stability at 0.5 A g^{-1} due to the component and structural advantages. Our work not only provides a facile synthesis method for high-entropy compounds but also offers a deliberate control strategy for the HEMO structure to improve its performance, which will bring great potential for HEMOs as high-performance materials in energy storage and conversion.

Results and discussion

The amorphous-to-crystalline strategy we propose to simultaneously realize the facile synthesis of high-entropy metal oxides (HEMOs) and their structure regulation requires two steps: a hydrothermal reaction for acquiring amorphous carbon spheres loaded with five metal species, and a calcination oxidation process transforming the amorphous precursor into crystalline high-entropy oxides with different structures. As shown in Fig. 1a, the mixed solution of glucose and equimolar amounts of five metal salts can be transformed into the spherical carbon precursor loaded with five metal species under hydrothermal conditions at 160 °C for 12 h. During the reaction, glucose not only acts as the carbon source responsible for the formation of amorphous carbon spheres when no metal salts are used, as confirmed by the scanning electron microscopy (SEM) image and X-ray diffraction (XRD) pattern in Fig. S1,† but it also possesses powerful chelation capacity due to the abundance of –OH functional groups to adsorb the various metallic ions into carbon spheres. After that, the spherical amorphous carbon precursors with five metal species were transformed to crystalline HEMOs through calcination at high temperatures in air. By deliberately designing the heat treatment in the process of calcination–oxidation, the HEMO structure transforms from solid spheres to core–shell spheres, and then to hollow spheres as the temperature increases to adjust the ion diffusion and oxidation rates.

Due to the powerful chelation capacity of the –OH functional groups, glucose can chelate many metal ions, which means that hydrothermal treatment of the mixture of glucose and different metal salts is a universal route for the formation of amorphous carbon loaded with different metal species. Similarly, heat treatment adjustment to vary the ion diffusion and oxidation rates is also universally used to control the material structure.[30,31] Thus, our amorphous-to-crystalline transformation strategy presents a universal technique by which to achieve the simultaneous realization of the facile synthesis and structure regulation of HEMOs.

Fig. 1b–q display SEM images of the amorphous precursors and their corresponding calcination crystalline products with four different groups of five metals: Cr–Mn–Fe–Co–Ni, Cr–Mn–Fe–Ni–Cu, Cr–Mn–Fe–Ni–Zn and Cr–Mn–Co–Ni–Cu, which clearly demonstrate the universality of the amorphous-to-crystalline transformation strategy. To clearly show the structural evolution of the HEMOs, transmission electron microscopy (TEM) images of the corresponding four groups of HEMOs are displayed in Fig. 2 and S2.† It is obvious that the precursors are composed of solid spheres, and the structures of HEMOs evolve from solid spherical structure to core–shell structure and then to hollow structure with the increase of calcining temperature. Here, the as-synthesized high-entropy CrMnFeCoNiO products are chosen as examples for detailed discussions.

Fig. S1b† displays a SEM image of the CrMnFeCoNi@C precursor, which is composed of microspheres with diameters of 1–3 μm. Fig. 2a shows a TEM image and corresponding EDS elemental mappings of the precursor. It can be clearly observed that the precursor is solid carbon sphere with five kinds of metallic ions (Cr, Mn, Fe, Co and Ni) evenly distributed in the entire sphere. Its XRD pattern in Fig. S1c† confirms its amorphous nature.

After the calcination-oxidation, amorphous carbon solid spheres with five metal species are successfully transformed to crystalline HEMOs with different structures, including solid

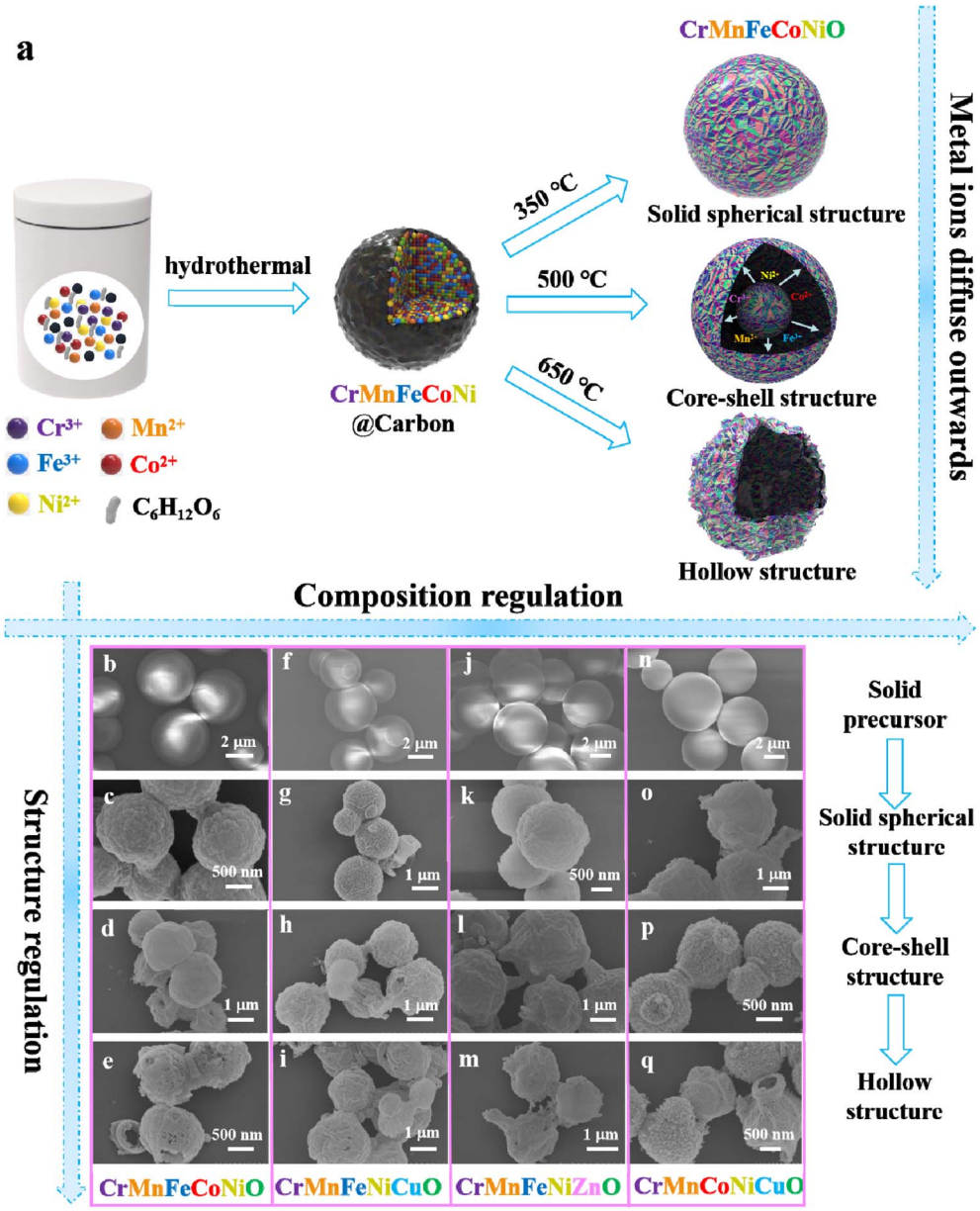

Fig. 1 (a) Schematic illustrations of the synthesis process of HEMOs through the amorphous-to-crystalline transformation strategy; (b–q) composition and structure regulation of HEMOs through the amorphous-to-crystalline transformation strategy.

spherical structure, core–shell structure, and hollow structure, by temperature control. Fig. S3† and 2b–d show SEM and TEM images and the corresponding EDS elemental mappings of the products prepared by calcining the amorphous carbon spheres at 350 °C, 500 °C and 650 °C, respectively. From the SEM images, all three products consist of spherical particles, similar to the precursors. But from the TEM images in Fig. 2b–d, they appear totally different. The product prepared at 350 °C has solid spherical structure (s-CrMnFeCoNiO), at 500 °C core–shell structure (c-CrMnFeCoNiO), while at 650 °C hollow structure (h-CrMnFeCoNiO), demonstrating the successful structure regulation on the HEMOs. The hollow structure has a thin layer of HEMOs on the sphere's surface. The layers are very thin and appear like wavy film. Similar results can be also observed in the CrMnFeNiCuO, CrMnFeNiZnO and CrMnCoNiCuO hollow structures shown in Fig. S2.† From the EDS elemental mapping images, all the metal elements and oxygen are uniformly distributed in the entire product, suggesting the homogeneous nature of the HEMOs. ICP test of c-CrMnFeCoNiO also confirms the coexistence of the five metal elements with atom percentages of 24.5%, 19.3%, 17.1%, 18.9% and 20.2%, respectively. It can be also observed that with increased calcination temperature, the metal ions tend to diffuse outwards with different diffusion rates, which corresponds to the structure transition from solid to hollow structure.[32] Compared with Cr and Mn ions, the diffusion rates of Ni, Co and Fe are faster. However, when the temperature is too high (such as 800 °C), the spherical structure collapses and phase separation occurs in the final

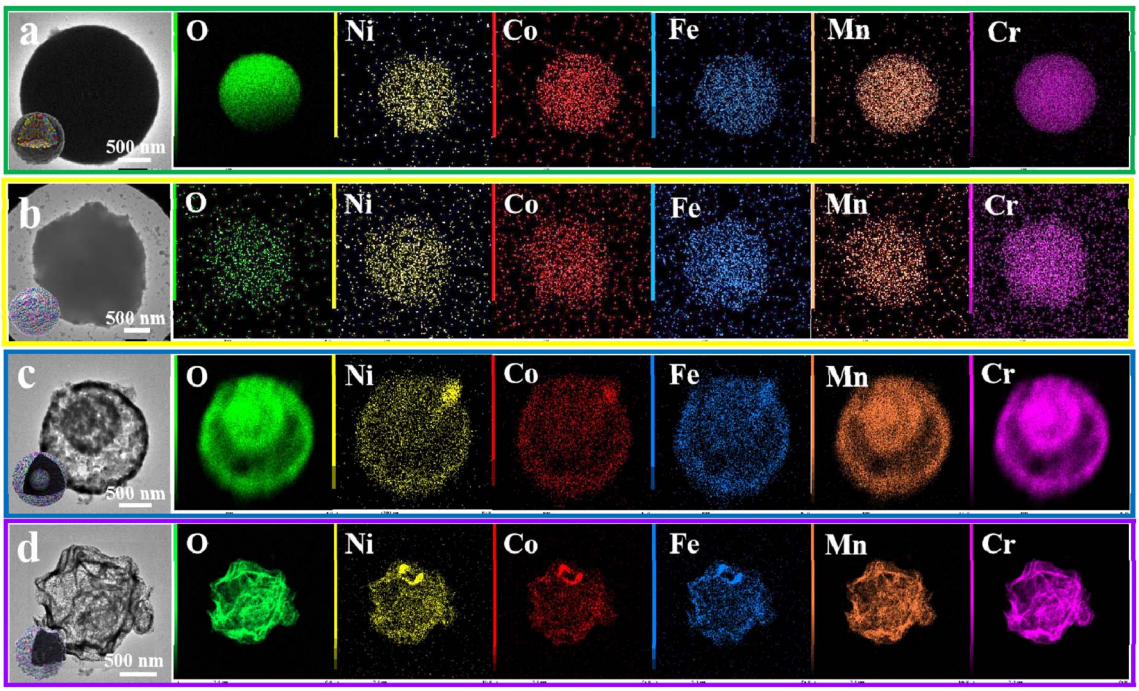

Fig. 2 TEM images and the corresponding element EDS mappings of (a) amorphous precursor, (b) solid CrMnFeCoNiO spheres, (c) core–shell CrMnFeCoNiO spheres, and (d) hollow CrMnFeCoNiO spheres.

product (Fig. S4a and b†). The structure evolution of the HEMO spheres is summarized in Fig. 3a. At high calcination temperatures in air, the amorphous carbon is oxidized to carbon oxide, and only the metallic skeleton can be preserved. The metals react with oxygen to form crystalline HEMOs. During this amorphous-to-crystalline process, oxygen diffuses inwards and

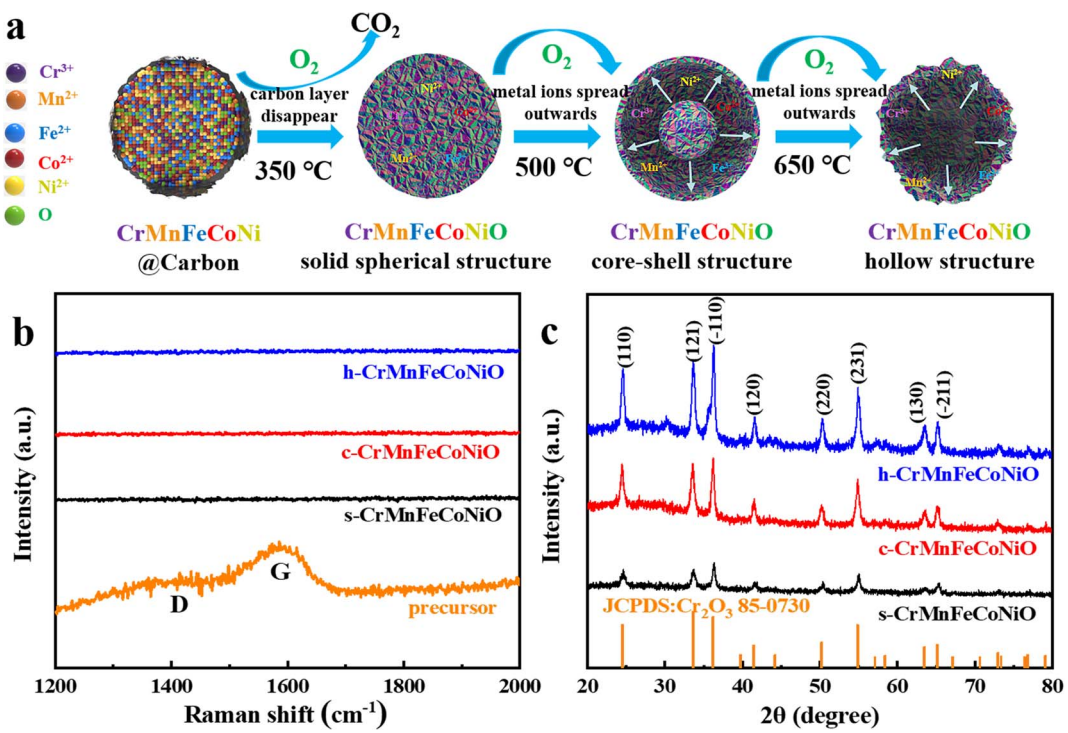

Fig. 3 (a) Synthesis mechanism scheme; (b) Raman spectra and (c) XRD patterns of the precursor, s-CrMnFeCoNiO, c-CrMnFeCoNiO and h-CrMnFeCoNiO.

the metal species outwards to react with each other, and the diffusion rate at different temperatures determines the final structure of the HEMOs. When the temperature is low, the diffusion rate of the metallic species is too low to diffuse outwards, resulting in the formation of solid spheres. With the temperature increasing, the diffusion rate increases, making the structure transform from solid spherical structure to core–shell structure to hollow structure.

The elimination of amorphous carbon is demonstrated by the Raman spectra in Fig. 3b. In the Raman spectrum of the precursor, there are two peaks at 1383 cm^{-1} and 1592 cm^{-1} corresponding to the D and G bands of carbon, respectively, confirming the existence of carbon in the precursor. After calcination, no peaks can be observed in the Raman spectra of all three CrMnFeCoNiO products, demonstrating that the amorphous carbon has been completely removed, leaving only the oxide skeleton after the oxidation reactions. The single-phase nature of the obtained HEMOs was further investigated by XRD. Fig. 3c shows the XRD patterns of the s-CrMnFeCoNiO, c-CrMnFeCoNiO and h-CrMnFeCoNiO samples, revealing that all the products have the same cubic phase, consistent with JCPDS No. 85-0730. Specifically, the diffraction peaks at around 24.5°, 33.6°, 36.2°, 41.5°, 50.2°, 54.5°, 63.4° and 65.1° of c-CrMnFeCoNiO can be indexed to (110), (121), (−110), (120), (220), (231), (130) and (−211), and no other diffraction peaks arising from other oxides or impurities can be detected, demonstrating that no phase separation occurs in the product, which is consistent with the results of EDS elemental mappings. Fig. S5† displays TEM and HRTEM images of a single core–shell sphere. The HRTEM images in different regions in Fig. S5b and c† clearly reveal that the structure is composed of a lot of crystalline nanoparticles. These crystalline nanoparticles exhibit lattice fringes in different directions with spacings of 0.363 nm or 0.266 nm, corresponding to (110) or (121) of cubic oxide phase (JCPDS No. 85-0730). This result further demonstrates that through the amorphous-to-crystalline strategy, the amorphous precursor was successfully transformed to HEMOs with high crystallinity. In addition, the XRD patterns of other HEMOs, including CrMnFeNiCuO, CrMnFeNiZnO, CrMnCoNiCuO and CrMnCoNiZnO, through the amorphous-to-crystalline strategy in Fig. S6,† all show a similar pattern to JCPDS No. 85-0730, demonstrating the formation of high-entropy oxides and the universality of the strategy. Moreover, in order to further prove the universality of this method, four other kinds of transition metal oxides, including monometallic oxide (CrO), bimetallic oxide (CrMnO), trimetallic oxide (CrMnFeO) and tetrametallic oxide (CrMnFeCoO), have also been prepared through a similar procedure, and they all have the same phase structure as the CrMnFeCoNiO with similar morphologies (Fig. S7†).

X-ray photoelectron spectroscopy (XPS) was further performed to study the valence states and surface chemical compositions of the HEMOs. Fig. 4 displays the high-resolution XPS spectra for Cr, Mn, Fe, Co, Ni, and O in the obtained c-CrMnFeCoNiO. In the Cr 2p spectrum (Fig. 4a), the peaks of Cr $2p_{3/2}$ and Cr $2p_{1/2}$ can be divided into four specific peaks; the peaks at 576.4 eV and 585.8 eV correspond to Cr(III), while the peaks at 578.7 eV and 587.5 eV correspond to Cr(VI).[33,34] The Mn 2p spectrum in Fig. 4b exhibits four peaks deconvoluted to Mn(III) and Mn(IV) at $2p_{1/2}$ of 656.4 eV and 654.2 eV and at $2p_{3/2}$ of 644.3 eV and 641.7 eV, respectively.[35] The two peaks in the Fe 2p spectrum (Fig. 4c) can be assigned to Fe(III) $2p_{1/2}$ (725.7 eV) and Fe(III) $2p_{3/2}$ (711.3 eV).[36] The Co 2p spectrum in Fig. 4d displays the existence of metallic Co at 792.9 eV and 772.9 eV. Peaks at 798.2 eV and 781.7 eV, along with two satellite peaks at 805.5 eV and 788.3 eV, are fitted with Co $2p_{1/2}$ and Co $2p_{3/2}$ of the oxidized Co species, respectively.[37] There are two peaks at 864.9 eV and 851.7 eV in the Ni 2p spectrum (Fig. 4e), which can be assigned to Ni $2p_{1/2}$ and Ni $2p_{3/2}$, respectively, while the other peaks are attributed to the satellite and the oxidized Ni species on the sample surface.[38–40] In Fig. 4f, the O 1s spectrum is deconvoluted into three peaks at 533.2 eV, 531.8 eV, and 530.1 eV. The main peak at 530.1 eV can be attributed to metal oxides (M-O), while the other two are assigned to the C–O and C=O environment.[41] All the XPS results manifest the co-existence of the five metal elements and oxygen in the final product, well consistent with the EDS elemental mappings and demonstrating once again the formation of the HEMO. Furthermore, in order to observe the difference caused by the structure change, the XPS spectra of c-CrMnFeCoNiO are compared with s-CrMnFeCoNiO and h-CrMnFeCoNiO. As shown in Fig. S8,† the peaks of most metal elements in c-CrMnFeCoNiO shift to higher binding energies, implying that they are in higher valence state and can provide higher capacity in the redox reaction of the electrode materials. Meanwhile, the change of binding energy affects the electronic structure between metals, increasing the number of active sites and boosting the synergistic effect between metals, which would be beneficial for electrocatalytic LIB performance.

Core–shell structures with nanoscale hollow interiors and functional shells have great technological significance in energy storage and conversion, including LIBs.[42,43] In this study, the obtained high-entropy CrMnFeCoNiO materials were applied as anode for LIBs. Cyclic voltammetry (CV) was performed to investigate the electrochemical redox reactions of the CrMnFeCoNiO anodes. As shown in Fig. 5a, because of the insertion and extraction of Li^+, there are several anodic and cathodic peaks in the curves. During the first cycle discharge, a strong reduction peak is observed at 0.5 V, originating from the reduction reaction of Cr, Mn, Fe, Co, Ni ions and the formation of solid electrolyte interphase (SEI) film on the electrode surface, which is the main cause of irreversible capacity loss in discharge process. In this process, the high-entropy transition metal oxides are reduced to simple metals, and amorphous Li_2O is formed. In the first positive (lithiation) scan, a wide oxidation peak appears near 1.5–1.8 V, corresponding to the oxidation process of the metals. As the cycling proceeds, the peak intensity of the cathode peak and anode peak decreases due to the irreversible reaction of the electrode in the charge and discharge process. The CV curves of the c-CrMnFeCoNiO anode overlap from the second to the fifth turn, indicating that the material has good reversibility in the electrochemical reaction process. Fig. 5b displays the charge–discharge curve of the c-CrMnFeCoNiO anode at the voltage range of 0.01–3 V and

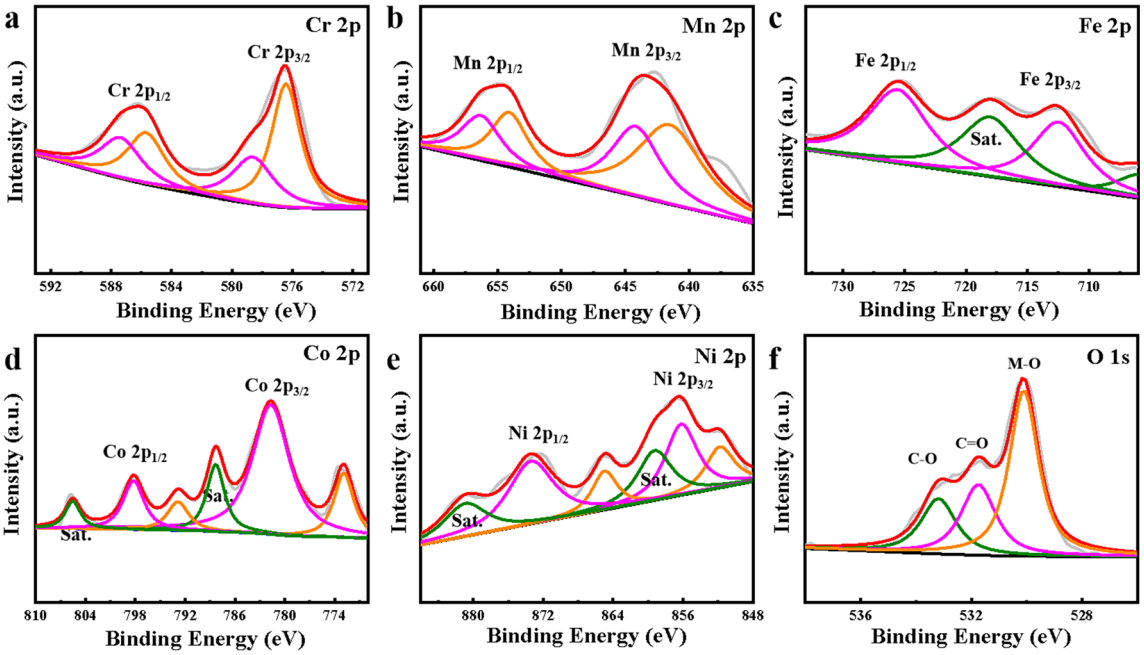

Fig. 4 High-resolution XPS spectra of c-CrMnFeCoNiO: (a) Cr 2p; (b) Mn 2p; (c) Fe 2p; (d) Co 2p; (e) Ni 2p and (f) O 1s.

the current density of 0.5 A g^{-1}. Its initial discharge capacity and initial charge capacity are 1415.6 mA h g^{-1} and 1041.2 mA h g^{-1}, respectively, and the coulombic efficiency can reach 73.6%.

To explore the impact of structural differences, the cycling performances of the three high-entropy transition metal oxides were investigated and are shown in Fig. 5c. It can be seen that the coulombic efficiencies of s-CrMnFeCoNiO, c-CrMnFeCoNiO and h-CrMnFeCoNiO are all close to 100% after 100 cycles. Among the three HEMOs with different structures, c-CrMnFeCoNiO has the highest specific capacity. It delivers a high specific discharge capacity of 1415.6 mA h g^{-1} in the first cycle, which decreases during the first several cycles, attributed to SEI formation and Li^+ trapping in the oxide framework. It remains stable and then increases due to an activation process by releasing the trapped Li^+, and then reaches a specific capacity of 968.5 mA h g^{-1} at the 100th cycle, which manifests the great recyclability of the core–shell structure. In order to delve deeper into performance discrepancies, the galvanostatic rate

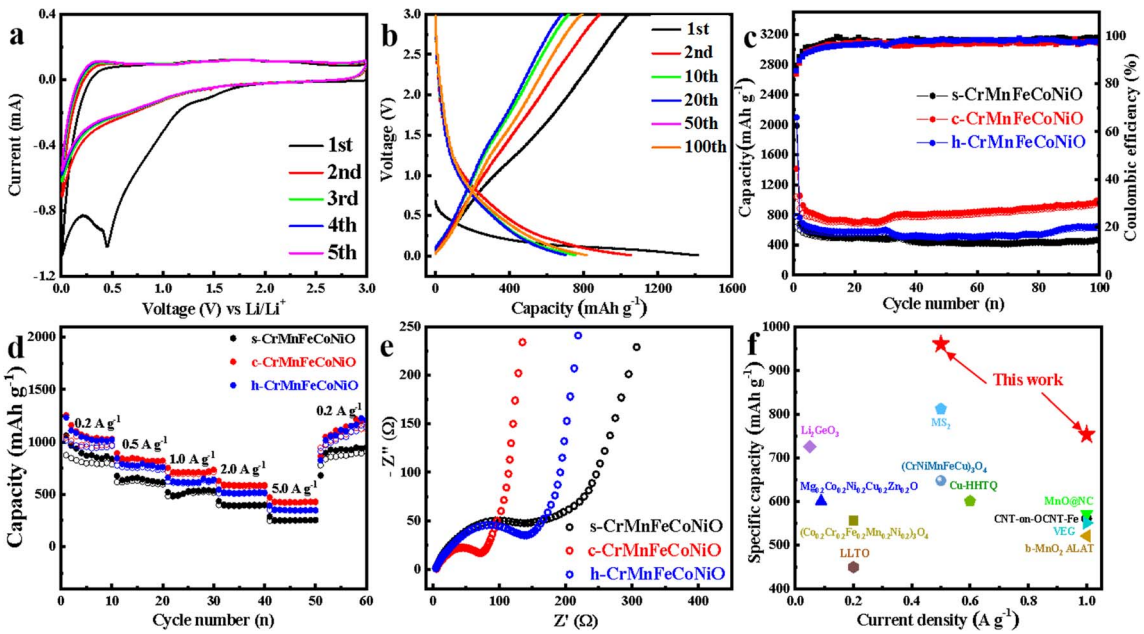

Fig. 5 (a) CV curves and (b) initial galvanostatic charge–discharge curves at 0.5 A g^{-1} of c-CrMnFeCoNiO; (c) cycling performance curves; (d) rate capability; (e) electrochemical impedance spectroscopy of s-CrMnFeCoNiO, c-CrMnFeCoNiO, and h-CrMnFeCoNiO; (f) LIB performance comparison of c-CrMnFeCoNiO with recently reported LIB anodes.

capability performances of the different HEMOs at different currents are presented in Fig. 5d. The c-CrMnFeCoNiO delivers the largest specific capacity at any current density. It is demonstrated that the product with core–shell structure has the best charge–discharge performance in comparison to the solid and the hollow spherical structure, which confirms again the significance of structure regulation on the high-entropy compounds. When the current density returns to the initial value, the specific capacities of the batteries assembled with the three HEMOs return to the initial level or even better, which further confirms that our electrode materials are basically unaffected by external conditions such as charge and discharge current density, and have practical application value. Electrochemical impedance spectroscopy (EIS; Fig. 5e) tests indicate that the c-CrMnFeCoNirO electrode has the minimum electrochemical impedance and best conductivity, which is consistent with the previous test results and further reveals the advantage of the core–shell structure.

Moreover, in order to demonstrate the advantage of high-entropy effect on LIB performance, ternary and quaternary transition metal oxides c-CrMnFeO, c-CrFeCoNiO, c-CrMnCoNiO, c-CrMnFeNiO and c-CrMnFeCoO were also synthesized by the amorphous-to-crystalline transformation process. Fig. 6a and b display their galvanostatic rate capability performance and electrochemical impedance spectroscopy test along with those of the high-entropy c-CrMnFeCoNiO, clearly revealing that the increase of element types can greatly improve the high-entropy effect and activity of the material, and thus enhance the lithium electrochemical properties. The capacities of c-CrMnFeCoNiO during charging and discharging were also tested under high current densities. Fig. S9† displays the rate capacities of c-CrMnFeCoNiO under the high current densities of 1, 2, 5, 10 and even up to 20 A g^{-1} in comparison with several quaternary transition metal oxides. c-CrMnFeCoNiO can deliver the specific capacities of 510.9 mA h g^{-1}, 364.9 mA h g^{-1} and 228.3 mA h g^{-1} at 5, 10 and 20 A g^{-1}, respectively, much higher than those of the quaternary transition metal oxides. When the current density returns to 1 A g^{-1} after charging and discharging at the current densities of 1, 2, 5, 10 and 20 A g^{-1}, the specific capacity is restored to approximatively the initial level, confirming that c-CrMnFeCoNiO also has great rate capability under high current densities. Fig. S9† also displays the rate capacities of the quaternary transition metal oxides for comparison. It can be observed that the capacities of these quaternary transition metal oxides at different current densities are similar to each other, but much smaller than those of the HEMOs (c-CrMnFeCoNiO), which clearly reveals that the increase of element species can greatly enhance the lithium storage properties. Finally, the long-term cycling stability of the c-CrMnFeCoNiO electrode was evaluated, and the data obtained at a charge–discharge rate of 0.5 A g^{-1} for 300 cycles are shown in Fig. 6c. After a series of high-rate charge–discharge cycling processes, the inside of the HEMO structure realizes complete penetration of the electrolyte, and the capacity increases. The

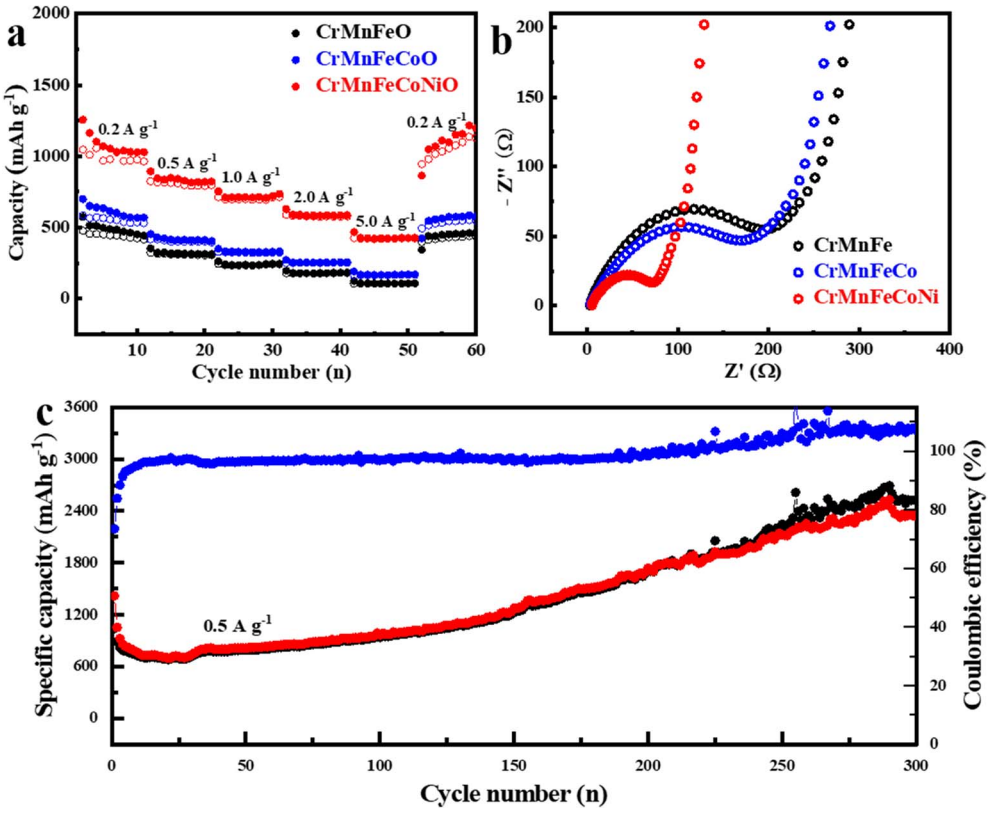

Fig. 6 (a) Rate capability and (b) electrochemical impedance spectroscopy of c-CrMnFeO, c-CrMnFeCoO and c-CrMnFeCoNiO; (c) long-term cycling stability of the c-CrMnFeCoNiO anode.

increase of capacity illustrates the excellence of the core–shell structure. Furthermore, the charge and discharge capacities increase greatly after 150 cycles, which might be attributed to the pseudo-capacitive interfacial storage. As reported, the decomposition products of the electrolyte (1.0 M $LiPF_6$ in EC : DMC : EMC = 1 : 1 : 1 vol%) grow on the surface of active materials, forming polymeric/gel-like films.[44,45] The core–shell structure makes the decomposition products easily accumulate on the active materials, providing the extra capacity as cycling goes on until coulombic efficiency is obviously higher than 100% after 250 cycles. In general, all the high-entropy CrMnFeCoNiO transition metal oxides synthesized in this study have excellent LIB performances. Among them, the core–shell HEMOs structure has the most active sites, best battery activity and stability due to its structural advantages and is superior to many reported oxide and high-entropy oxide lithium electrode materials (Fig. 5f and Table S1†). Because of its universal fabrication and excellent performance, the high-entropy core–shell c-CrMnFeCoNiO structure would have great application potential to serve as a promising electrode material for future high-performance LIBs.

Conclusions

In summary, a general amorphous-to-crystalline transformation route is proposed to simultaneously achieve the synthesis of high-entropy transition metal oxides and regulate their structure. During the formation of amorphous carbon spheres from glucose under hydrothermal conditions, various metal ions can be homogeneously loaded due to the powerful chelation capacity of the many –OH functional groups in glucose. The subsequent calcination and oxidation treatment of the amorphous precursor leads to the transformation of the amorphous spheres to crystalline HEMOs. More importantly, with the increase of calcination temperature, the HEMOs' structure evolves from solid spherical structure to core–shell structure and then to hollow structure due to the different ion diffusion and oxidation rates at different temperatures. Furthermore, this strategy can be extended to the preparation of various oxides, including different high-entropy oxides of various components. As an example, due to the component and structural advantages, the core–shell high-entropy CrMnFeCoNiO exhibits excellent lithium storage performance with high specific capacity, low electrochemical impedance and fast Li^+ conductivity. This study not only provides a low-cost and efficient synthesis route for high-entropy compounds, but also presents a rational concept for their difficult structure regulation, giving HEMOs great potential as high-performance materials in energy storage and conversion.

Experimental

Materials

All the reagents used were of analytical grade and used as received. Nickel chloride ($NiCl_2 \cdot 6H_2O$), cobalt chloride ($CoCl_2 \cdot 6H_2O$), ferric chloride ($FeCl_3$), manganese chloride ($MnCl_2 \cdot 4H_2O$), chromium chloride ($CrCl_3 \cdot 6H_2O$), and glucose ($C_6H_{12}O_6$) were purchased from Sinopharm Chemical Reagent Co. Ltd.

Synthesis of precursor spheres

In a typical procedure, 1.8 g of $C_6H_{12}O_6$ was added to 30 mL of deionized water. After 10 minutes of magnetic stirring, 0.165 mmol of $NiCl_2 \cdot 6H_2O$, 0.165 mmol of $CoCl_2 \cdot 6H_2O$, 0.165 mmol of $FeCl_3$, 0.165 mmol of $MnCl_2 \cdot 4H_2O$ and 0.165 mmol of $CrCl_3 \cdot 6H_2O$ were added to form a uniform solution. The resulting solution was then transferred into a Teflon-lined stainless steel autoclave and kept at 160 °C for 12 h. After cooling to room temperature, the precipitate was collected and washed with deionized water and absolute ethanol three times, respectively. Finally, the product was dried overnight at 80 °C, and the precursor spheres were obtained.

Synthesis of high-entropy metal oxides (CrMnFeCoNiO) with different structures

The obtained precursor spheres were heated in air with a 3 °C min^{-1} ramping rate in a muffle furnace and kept at 350 °C for 2 h to transform to the solid s-CrMnFeCoNiO spherical structure. The core–shell c-CrMnFeCoNiO and hollow h-CrMnFeCoNiO structures were synthesized at 500 °C and 650 °C for 2 h in a muffle furnace, respectively.

Synthesis of c-CrO, c-CrMnO, c-CrMnFeO and c-CrMnFeCoO

These samples were synthesized through the same procedure as HEMO c-CrMnFeCoNiO spheres with the addition of the corresponding metal sources.

Characterization

X-ray diffraction (XRD) patterns of the materials were collected on a Shimadzu XRD-6000 powder X-ray diffractometer with Cu K_α radiation. Transmission electron microscopy (TEM), high-resolution TEM (HRTEM) images and energy-dispersive X-ray spectroscope (EDS) elemental mappings of the samples were obtained on a JEOL JEM-2800 transmission electron microscope. Scanning electron microscopy (SEM) images of the products were acquired on a scanning electron microscope. X-ray photoelectron (XPS) spectra were detected with a PHI-5000 Versa Probe X-ray photoelectron spectrometer using an Al K_α X-ray source.

Electrochemical measurements

All of the working electrodes consisted of active materials (40%), a few layers of graphene (40%), super P (10%) and PVDF (10%) as a binder, which were painted on a Cu current collector dried at 60 °C for 12 h under vacuum. The mass loading of the active material is about 0.083 mg cm^{-2}. The coin-type cells (CR 2032) were assembled in an Ar-filled glove box where O_2 and H_2O concentrations were <1 ppm. Li-metal wafers served as a positive electrode, 1.0 M $LiPF_6$ in EC : DMC : EMC = 1 : 1 : 1 vol% was used as an electrolyte, and a porous polypropylene paper (PP, Celgard 2400) as a separator. The discharge–charge measurements, including cycling performance and rate

stability, were carried out on a battery testing system (Land, Wuhan, China) in a voltage range of 0.01–3.0 V. Cyclic voltammetry measurements were performed at various scan rates with a voltage window from 0.01–3.0 V *vs.* Li/Li^+ on an electrochemical CHI760D workstation (Chenhua, Shanghai, China). EIS measurements were carried out on CHI760D with a 5 mV amplitude of the AC signal at a frequency range of 100 kHz to 0.01 Hz.

Data availability

We have included all of the data used for this manuscript in the paper's body or the ESI.†

Author contributions

D. W. L. and L. L. performed the synthesis and electrochemical test of the high-entropy transition metal oxides. M. F. S. and Q. L. K. performed TEM, HRTEM and EDS investigations of the high-entropy transition metal oxides. F. G. and Q. Y. L. supervised the project and wrote the manuscript, with input from all the authors.

Conflicts of interest

The authors declare no competing interests.

Acknowledgements

This work was supported by the National Natural Science Foundation of China (Grant No. 21871130, 22175084 and 22275082) and the Scientific and Technological Innovation Project of Carbon Emission Peak and Carbon Neutrality of Jiangsu Province (Grant No. BE2022024).

References

1 M. Li, J. Lu, Z. W. Chen and K. Amine, 30 years of lithium-ion batteries, *Adv. Mater.*, 2018, **30**, 1800561.
2 J. Xie and Y. C. Lu, A retrospective on lithium-ion batteries, *Nat. Commun.*, 2020, **11**, 2499.
3 C. N. Gannett, J. Kim, D. Tirtariyadi, P. J. Milner and H. D. Abruna, Investigation of ion-electrode interactions of linear polyimides and alkali metal ions for next generation alternative-ion batteries, *Chem. Sci.*, 2022, **13**, 9191–9201.
4 S. K. Jung, I. Hwang, D. Chang, K. Y. Park, S. J. Kim, W. M. Seong, D. Eum, J. Park, B. Kim, J. Kim, J. H. Heo and K. Kang, Nanoscale phenomena in lithium-ion batteries, *Chem. Rev.*, 2020, **120**, 6684–6737.
5 R. H. Yu, S. B. Li, G. N. Chen, C. Zuo, B. H. Zhou, M. L. Ni, H. Y. Peng, X. L. Xie and Z. G. Xue, Monochromatic "photoinitibitor"-mediated holographic photopolymer electrolytes for lithium-ion batteries, *Adv. Sci.*, 2019, **6**, 1900205.
6 Z. J. Wang, Y. Y. Wang, C. Wu, W. K. Pang, J. F. Mao and Z. P. Guo, Constructing nitrided interfaces for stabilizing Li metal electrodes in liquid electrolytes, *Chem. Sci.*, 2021, **12**, 8945–8966.
7 Q. Chen, X. F. Tan, Y. G. Liu, S. B. Liu, M. F. Li, Y. L. Gu, P. Zhang, S. J. Ye, Z. Z. Yang and Y. Y. Yang, Biomass-derived porous graphitic carbon materials for energy and environmental applications, *J. Mater. Chem. A*, 2020, **8**, 5773–5811.
8 J. P. Pender, G. Jha, D. H. Youn, J. M. Ziegler, I. Andoni, E. J. Choi, A. Heller, B. S. Dunn, P. S. Weiss, R. M. Penner and C. B. Mullins, Electrode degradation in lithium-ion batteries, *ACS Nano*, 2020, **14**, 1243–1295.
9 H. Tavassol, E. M. C. Jones, N. R. Sottos and A. A. Gewirth, Electrochemical stiffness in lithium-ion batteries, *Nat. Mater.*, 2016, **15**, 1182–1187.
10 L. C. Yue, J. Liang, Z. G. Wu, B. H. Zhong, Y. L. Luo, Q. Liu, T. S. Li, Q. Q. Kong, Y. Liu, A. M. Asiri, X. D. Guo and X. P. Sun, Progress and perspective of metal phosphide/carbon heterostructure anodes for rechargeable ion batteries, *J. Mater. Chem. A*, 2021, **9**, 11879–11907.
11 W. M. Seong, K. Y. Park, M. H. Lee, S. Moon, K. Oh, H. Park, S. Lee and K. Kang, Abnormal self-discharge in lithium-ion batteries, *Energy Environ. Sci.*, 2018, **11**, 970–978.
12 A. M. Bates, Y. Preger, L. Torres-Castro, K. L. Harrison, S. J. Harris and J. Hewson, Are solid-state batteries safer than lithium-ion batteries?, *Joule*, 2022, **6**, 742–755.
13 A. Manthiram, A reflection on lithium-ion battery cathode chemistry, *Nat. Commun.*, 2020, **11**, 1550.
14 X. N. Feng, D. S. Ren, X. M. He and M. G. Ouyang, Mitigating thermal runaway of lithium-ion batteries, *Joule*, 2020, **4**, 743–770.
15 Y. G. Yao, Z. N. Huang, P. F. Xie, S. D. Lacey, R. J. Jacob, H. Xie, F. J. Chen, A. M. Nie, T. C. Pu, M. Rehwoldt, D. W. Yu, M. R. Zachariah, C. Wang, R. Shahbazian-Yassar, J. Li and L. B. Hu, Carbothermal shock synthesis of high-entropy-alloy nanoparticles, *Science*, 2018, **359**, 1489–1494.
16 T. A. A. Batchelor, J. K. Pedersen, S. H. Winther, I. E. Castelli, K. W. Jacobsen and J. Rossmeisl, High-entropy alloys as a discovery platform for electrocatalysis, *Joule*, 2019, **3**, 834–845.
17 Q. Q. Ding, Y. Zhang, X. Chen, X. Q. Fu, D. K. Chen, S. J. Chen, L. Gu, F. Wei, H. B. Bei, Y. F. Gao, M. R. Wen, J. X. Li, Z. Zhang, T. Zhu, R. O. Ritchie and Q. Yu, Tuning element distribution, structure and properties by composition in high-entropy alloys, *Nature*, 2019, **574**, 223–227.
18 Z. X. Cai, H. Goou, Y. Ito, T. Tokunaga, M. Miyauchi, H. Abe and T. Fujita, Nanoporous ultra-high-entropy alloys containing fourteen elements for water splitting electrocatalysis, *Chem. Sci.*, 2021, **12**, 11306–11315.
19 E. P. George, D. Raabe and R. O. Ritchie, High-entropy alloys, *Nat. Rev. Mater.*, 2019, **4**, 515–534.
20 C. R. McCormick and R. E. Schaak, Simultaneous multication exchange pathway to high-entropy metal sulfide nanoparticles, *J. Am. Chem. Soc.*, 2021, **143**, 1017–1023.
21 A. Sarkar, L. Velasco, D. Wang, Q. S. Wang, G. Talasila, L. de Biasi, C. Kübel, T. Brezesinski, S. S. Bhattacharya, H. Hahn

and B. Breitung, High entropy oxides for reversible energy storage, *Nat. Commun.*, 2018, **9**, 3400.

22 M. J. Cui, C. P. Yang, B. Y. Li, Q. Dong, M. L. Wu, S. Hwang, H. Xie, X. Z. Wang, G. F. Wang and L. B. Hu, High-entropy metal sulfide nanoparticles promise high-performance oxygen evolution reaction, *Adv. Energy Mater.*, 2021, **11**, 2002887.

23 M. D. Hossain, T. Borman, C. Oses, M. Esters, C. Toher, L. Feng, A. Kumar, W. G. Fahrenholtz, S. Curtarolo, D. Brenner, J. M. LeBeau and J. P. Maria, Entropy landscaping of high-entropy carbides, *Adv. Mater.*, 2021, **33**, 2102904.

24 D. W. Lai, Q. L. Kang, F. Gao and Q. Y. Lu, High-entropy effect of a metal phosphide on enhanced overall water splitting performance, *J. Mater. Chem. A*, 2021, **9**, 17913–17922.

25 C. M. Rost, E. Sachet, T. Borman, A. Moballegh, E. C. Dickey, D. Hou, J. L. Jones, S. Curtarolo and J. P. Maria, Entropy-stabilized oxides, *Nat. Commun.*, 2015, **6**, 8485.

26 Q. S. Wang, A. Sarkar, D. Wang, L. Velasco, R. Azmi, S. S. Bhattacharya, T. Bergfeldt, A. Düvel, P. Heitjans, T. Brezesinski, H. Hahn and B. Breitung, Multi-anionic and -cationic compounds: New high entropy materials for advanced Li-ion batteries, *Energy Environ. Sci.*, 2019, **12**, 2433–2442.

27 T. X. Nguyen, J. Patra, J. K. Chang and J. M. Ting, High entropy spinel oxide nanoparticles for superior lithiation–delithiation performance, *J. Mater. Chem. A*, 2020, **8**, 18963–18973.

28 J. Patra, T. X. Nguyen, C. C. Tsai, O. Clemens, J. Li, P. Pal, W. K. Chan, C. H. Lee, H. Y. T. Chen, J. M. Ting and J. K. Chang, Effects of elemental modulation on phase purity and electrochemical properties of Co-free high-entropy spinel oxide anodes for lithium-ion batteries, *Adv. Funct. Mater.*, 2022, **32**, 2110992.

29 B. Xiao, G. Wu, T. D. Wang, Z. G. Wei, Y. W. Sui, B. L. Shen, J. Q. Qi, F. X. Wei and J. C. Zheng, High-entropy oxides as advanced anode materials for long-life lithium-ion batteries, *Nano Energy*, 2022, **95**, 106962.

30 G. Q. Zhang and X. W. Lou, General synthesis of multi-shelled mixed metal oxide hollow spheres with superior lithium storage properties, *Angew. Chem., Int. Ed.*, 2014, **53**, 9041–9044.

31 Y. Huang, Y. J. Fang, X. F. Lu, D. Y. Luan and X. W. Lou, Co_3O_4 hollow nanoparticles embedded in mesoporous walls of carbon nanoboxes for efficient lithium storage, *Angew. Chem., Int. Ed.*, 2020, **59**, 19914–19918.

32 J. Y. Xu, H. Zhang, R. F. Wang, P. B. Xu, Y. L. Tong, Q. Y. Lu and F. Gao, Delicate control of multi-shelled Zn-Mn-O hollow microspheres as a high-performance anode for lithium-ion batteries, *Langmuir*, 2018, **34**, 1242–1248.

33 C. Z. Xu, Y. L. Xu, D. J. Zhong, H. X. Chang, J. X. Mou, H. Wang and H. Y. Shen, Zr^{4+} cross-linked chitosan-thiourea composite for efficient detoxification of Cr (VI) ions in aqueous solution, *Carbohydr. Polym.*, 2022, **296**, 119872.

34 Z. D. Wu, C. Zhao, W. G. Zeng, X. M. Wang, C. F. Liu, Z. Y. Yu, J. Zhang and Z. M. Qiu, Ultra-high selective removal of CR and Cr (VI) from aqueous solutions using polyethyleneimine functionalized magnetic hydrochar: Application strategy and mechanisms insight, *Chem. Eng. J.*, 2022, **448**, 137464.

35 X. Y. Lu, J. Pan, E. Lovell, T. H. Tan, Y. H. Ng and R. Amal, A sea-change: Manganese doped nickel/nickel oxide electrocatalysts for hydrogen generation from seawater, *Energy Environ. Sci.*, 2018, **11**, 1898–1910.

36 Y. J. Shih, Z. S. Chen, C. L. Chen, Y. H. Huang and C. P. Huang, Enhancing arsenic (III) removal by integrated electrocatalytic oxidation and electrosorption reactions on nano-textured bimetal composite of iron oxyhydroxide and manganese dioxide polymorphs (α-, γ-, β-, and ε-$Mn_xFe_{1-x}O$), *Appl. Catal., B*, 2022, **317**, 121757.

37 L. P. Zhong, T. Kropp, W. Baaziz, O. Ersen, D. Teschner, R. Schlögl, M. Mavrikakis and S. Zafeiratos, Correlation between reactivity and oxidation state of cobalt oxide catalysts for CO preferential oxidation, *ACS Catal.*, 2019, **9**, 8325–8336.

38 E. L. Hu, Y. F. Feng, J. W. Nai, D. Zhao, Y. Hu and X. W. Lou, Construction of hierarchical Ni-Co-P hollow nanobricks with oriented nanosheets for efficient overall water splitting, *Energy Environ. Sci.*, 2018, **11**, 872–880.

39 C. Du, L. Yang, F. L. Yang, G. Z. Cheng and W. Luo, Nest-like NiCoP for highly efficient overall water splitting, *ACS Catal.*, 2017, **7**, 4131–4137.

40 H. Yan, S. Yao, T. Zhang, D. L. Li, X. Y. Tang, M. X. Chen, Y. X. Zhou, M. R. Zhang, Y. B. Liu, X. Zhou, X. Feng, X. B. Chen and C. H. Yang, Promoting catalytic transfer hydrodecarbonylation of methyl stearate over bimetallic CoNi/HAP catalysts with strong electronic coupling effect, *Appl. Catal., B*, 2022, **306**, 121138.

41 L. Lin, K. Wang, A. Sarkar, C. Njel, G. Karkera, Q. S. Wang, R. Azmi, M. Fichtner, H. Hahn, S. Schweidler and B. Breitung, High-entropy sulfides as electrode materials for Li-ion batteries, *Adv. Energy Mater.*, 2022, **12**, 2103090.

42 Y. Lu, J. W. Nai and X. W. Lou, Formation of $NiCo_2V_2O_8$ yolk–double shell spheres with enhanced lithium storage properties, *Angew. Chem., Int. Ed.*, 2018, **57**, 2899–2903.

43 Z. Y. Wang, L. Zhou and X. W. Lou, Metal oxide hollow nanostructures for lithium-ion batteries, *Adv. Mater.*, 2012, **24**, 1903–1911.

44 S. J. Hao, B. W. Zhang, J. Y. Feng, Y. Y. Liu, S. Ball, J. S. Pan, M. Srinivasan and Y. Z. Huang, Nanoscale ion intermixing induced activation of Fe_2O_3/MnO_2 composites for application in lithium ion batteries, *J. Mater. Chem. A*, 2017, **5**, 8510–8518.

45 Y. Jin, L. Y. Dang, H. Zhang, C. Song, Q. Y. Lu and F. Gao, Synthesis of unit-cell-thick α-Fe_2O_3 nanosheets and their transformation to γ-Fe_2O_3 nanosheets with enhanced LIB performances, *Chem. Eng. J.*, 2017, **326**, 292–297.